Article

Fatigue improvement of AlSi10Mg fabricated by Laser-based powder bed fusion through heat-treatment.

Felix Sajadi*[1,3], Jan-Marc Tiemann[2], Nooshin Bandari[2], Ali Cheloee Darabi[3], Javad Mola[2], Siegfried Schmauder[3]

[1] Graduate School of Excellence advanced Manufacturing Engineering, University of Stuttgart
[2] Material Design and Structural Integrity Laboratory, Osnabrück University of Applied Sciences
[3] Institute for Materials Testing, Materials Science and Strength of Materials, University of Stuttgart
* Correspondence: felix.sajadi@imwf.uni-stuttgart.de

Abstract:

This study aims to identify an optimal heat-treatment parameter set for an additively manufactured AlSi10Mg alloy in terms of increasing the hardness and eliminating the anisotropic microstructural characteristics of the alloy in as-built condition. Furthermore, the influence of these optimized parameters on the fatigue properties of the alloy investigated. In this respect, microstructural characteristics of an AlSi10Mg alloy manufactured by Laser-Based Powder Bed Fusion in non-heat-treated and heat-treated conditions were investigated. Their static and dynamic mechanical properties were evaluated, and fatigue behavior was explained by a detailed examination of fracture surfaces. Much of the microstructure in the non-heat-treated condition was composed of columnar grains oriented parallel to the build direction. Further analysis revealed a high fraction of pro-eutectic α-Al. Through heat-treatment, the alloy was successfully brought to its peak-hardened condition, while eliminating the anisotropic microstructural features. Yield strength and ductility increased simultaneously after heat-treatment, which is due to the relief of residual stresses, preservation of refined grains, and introduction of precipitation strengthening. The fatigue strength, calculated at 10^7 cycles, improved as well after heat-treatment and finally detailed fractography reviled that a more ductile fracture mechanism has happened in the heat-treated condition compared to the non-heat-treated condition.

Keywords: Additive Manufacturing; mechanical properties; fatigue behavior; heat-treatment; aluminum alloys

1. Introduction

Laser-based powder bed fusion of metals (PBF-LB/M), also known as selective laser melting (SLM) as one of the highly promising additive manufacturing (AM) processes to produce light metal parts, is a feasible complement to conventional fabrication methods in various industries. PBF-LB/M enables the generation of parts by selectively scanning thin layers of powder metals with a laser beam based on a three-dimensional computer-aided design (CAD) model [1, 2]. Like other AM technologies, PBF-LB/M allows the production of individualized and geometrically complex shapes [3].

One of the commonly used alloys in PBF-LB/M processes is AlSi10Mg. This alloy offers a relatively high fluidity, low shrinkage as well as a reduced solidification temperature range, which results in better casting properties [4]. It is also classified within the age-hardenable alloys, as the addition of Mg enables the precipitation of nanoscale Mg_2Si particles and thus strengthening of the alloy [5]. To achieve the desired mechanical properties, heat-treatment is usually applied to reach a peak-hardened condition.

The excellent combination of low weight, high heat conductivity, and good mechanical properties has led to this alloy being used in many different applications such as aerospace and automotive industries [6, 7]. However, due to reliability concerns associated with the components, which are produced using PBF-LB/M, their application is

Preprints (www.preprints.org) | NOT PEER-REVIEWED | Posted: 2 April 2021 doi:10.20944/preprints202104.0075.v1

currently limited. One of the most important properties to be considered when evaluating materials for industrial applications is their fatigue behavior.

There exist a number of studies on the fatigue behavior of PBF-LB/M fabricated AlSi10Mg alloys. Aboulkhair et al. [8] investigated the influence of T6-heat-treatment with conventional treatment parameters as well as machining on the fatigue properties of AlSi10Mg alloys, reporting the highest fatigue property for specimens subjected to both T6-heat-treatment and surface machining. Mfusi et al. [9] revealed that the alloy exhibits better fatigue strength after stress relief, though all other mechanical properties obtained by the fabrication process deteriorate. Beretta et al. [10] have explored the effect of surface roughness as a result of building orientation on fatigue crack growth, demonstrating that there is a moderate correlation between surface roughness parameters and surface features measured by area, and a model was constructed to describe fatigue strength. Tang et al. [11] demonstrated the possibility of using extreme-value statistics to predict the fatigue life of additively manufactured as-built and heat-treated AlSi10Mg parts, with inputs of pore size distribution measured on a polished plane. Zhang et al. [12] looked on the effect of heat-treatment on the microstructure and fatigue life of PBF-LB/M manufactured AlSi10Mg. In all these cases, different process parameters, e.g., laser power, scanning speed, slicing thickness and the machine itself, were utilized to fabricate additively the samples. Furthermore, the following post-heat-treatment parameters, e.g., heat-treatment methods, timing and temperatures, varied from case to case as well. Since the modifications in microstructural characteristics and hence mechanical properties upon post-heat-treatment depend on the initial microstructure of an alloy, i.e., as-built, it is important to investigate the heat-treatment parameters and their intrinsic influences on a given alloy with a specific microstructure and further extent these investigations into the resulting mechanical properties.

The present study is firstly aimed at finding optimum heat-treatment parameters for our fabricated alloy in terms of increasing the harness and eliminating the anisotropic microstructural properties of the manufactured parts. Furthermore, the influence of optimized heat-treatment on the fatigue properties is investigated and finally, fracture surface analyses of the alloy is carried out.

2. Materials and Methods

2.1. PBF-LB/M fabrication and material

Since the main objective of this work is to investigate the influence of heat-treatment on microstructural characteristics and fatigue behavior of the AlSi10Mg alloy, the processing conditions and chemical composition were kept identical. The processing conditions, e.g., laser power, scanning speed, beam diameter, hatch space, and slice thickness, are listed in Table 1. A chess pattern with a field size of 5.89mm x 5.89mm. At each layer, the chess pattern was displaced by 4.02mm in X and 5.44mm in Y direction to suppress the microstructural anisotropy, that could otherwise arise from a unidirectional scanning strategy. To fabricate the materials, a TruPrint 3000 machine (TRUMPF GmbH + Co. KG) was utilized. The machine is equipped with a cylindrical build-chamber of Ø300mm x H400mm and a fiber laser with the maximum power of 500W. The build platform was heated to 200°C during the process to reduce residual stresses. Moreover, to minimize the oxidation, a nitrogen atmosphere with an oxygen content of <0.3% was applied during the process.

Table 1. Process parameters that were applied.

Laser power (W)	Scanning speed (mm/s)	Beam diameter (mm)	Hatch space (mm)	Slice thickness (mm)	Scanning strategy
420	1300	0.1	0.21	0.06	chess

The powder raw materials with particle sizes of 20 to 56μm (see Figure 1) were supplied by ECKA Granules Germany GmbH. The powders have a relatively high sphericity, 0.8±0.1, and roundness, 0.8±0.2, morphology. Sphericity is defined as the ratio of the particle surface area to the area of a sphere with the same volume and roundness is defined as the ratio of the average radius of curvature of the corners of the object to the radius of the maximum inscribed circle [13]. This morphological property favors better flowability of the powder during the recoating operation, more efficient particle packing, and formation of a highly dense powder bed, which yields a superior density, surface finish, and dimensional accuracy of the final fabricated component [14]. However, a few teardrop shaped powders as well as small satellites are also observed, which slightly reduce the flowability of the powder [15].

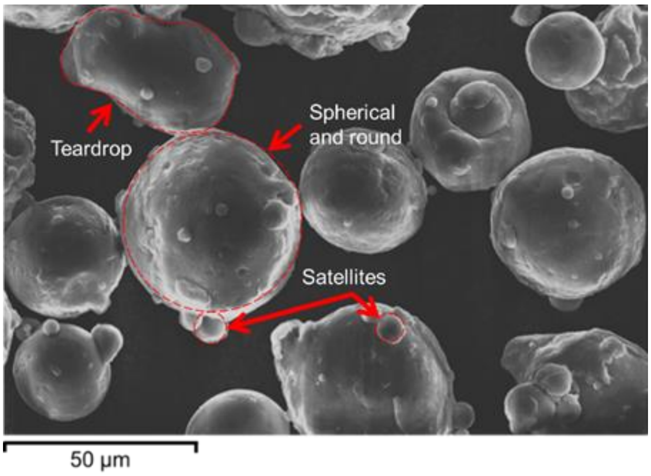

Figure 1. SEM image of the employed AlSi10Mg powder.

The chemical composition of the powder was kept constant (see Table 2) for all specimens and hence the conclusions of this study are valid only to this specific set of chemical and process condition.

Table 2. Chemical composition of the powder used for the fabrication of specimens in weight percentage.

Si	Mg	Fe	Cu	Mn	Ni	Zn	Pb	Sn	Ti	Al
0.9-1.1	0.2-0.45	0.55	0.05	0.45	0.05	0.1	0.05	0.05	0.15	balance

2.2. Specimen specification and finishing

To investigate the influence of heat-treatment on the flow and Wöhler (S-N) curves, round tensile and fatigue specimens were designed based on DIN 50125 and ASTM E606/E606M standards, respectively. In both cases, the radius of specimens manufactured directly by PBF-LB/M was one millimeter larger than the final dimensions for tests. After machining, specimens were brought to the final dimension with an arithmetic average surface roughness (Ra) of 2μm, thereby eliminating any irregular surface features, such as balling and satellites inherent to the PBF-LB/M manufacturing process (see Figure 2). It is believed that these surface defects reduce the fatigue strength of SLM parts [16]. In total, 6 tensile specimens and 30 fatigue specimens were fabricated. All specimens were fabricated with their length normal (90°) to the build platform surface. The Archimedes method and image processing of metallography cross-section images were used to measure the relative density of specimens. An average relative density of 99.2 ± 0.3% was measured for all specimens.

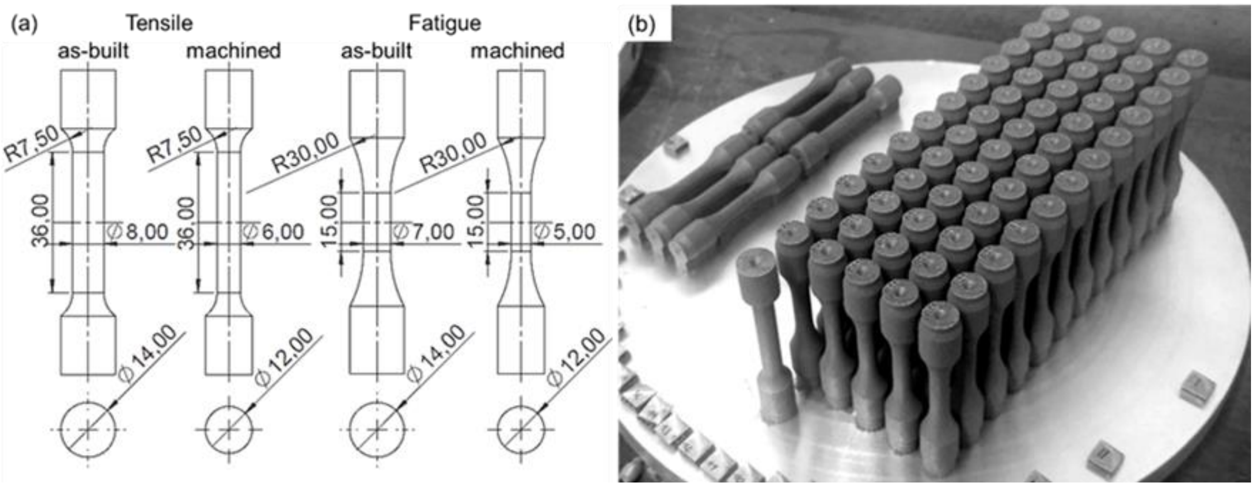

Figure 2. (a) Geometries of tensile and fatigue specimens before and after machining. (b) The position of specimens on the build-platform.

2.3. Heat-treatment

A heat-treatment procedure was designed based on the conventional T6 heat-treatment, to bring the alloy to its peak-hardened condition. To determine the peak-hardened condition, a series of parametric studies on small samples ($5x5x5mm^3$) were conducted (see Figure 3). The solution heat-treatment (SHT) were carried out for different times up to 2 hours at 300, 400, and 500°C. All samples were then quenched in water at room temperature. SHT was followed by artificial aging (AA) at 140, 160, and 180°C for times up to 48 hours (see Table 3). After identifying the optimized parameters, half of the tensile and fatigue specimens were subjected to the selected heat-treatment condition to be brought to the peak-hardened condition.

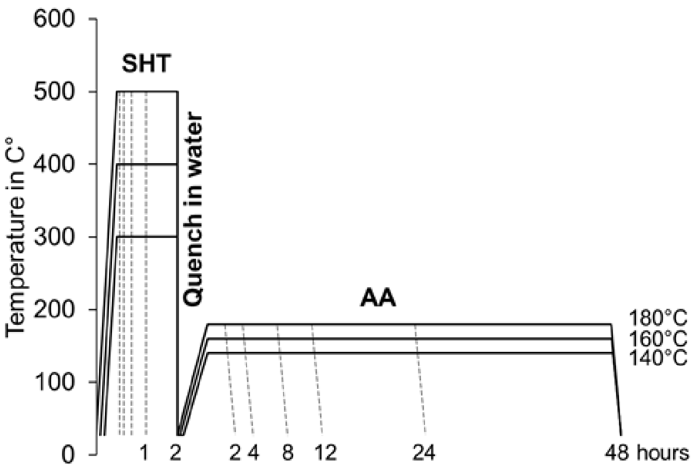

Figure 3. Schematic representation of the heat-treatment parametric study for both SHT and AA stages.

The Vickers micro hardness were measured under 600mN/14s loading condition, repeated 15 times and averaged. The tensile behavior was evaluated at room temperature and at a strain rate of $2x10^{-5}$ 1/s. Fatigue tests were performed under load-controlled condition, at a frequency of 20Hz and a stress ratio of R = -1. Both tensile and fatigue tests were performed using a 25kN machine (MTS Landmark®) equipped with an extensometer. In each condition, 3 tensile and 15 fatigue specimens were tested and averaged to account for statistical deviations.

Preprints (www.preprints.org) | NOT PEER-REVIEWED | Posted: 2 April 2021 doi:10.20944/preprints202104.0075.v1

Table 3. Heat-treatment conditions used in the parametric study.

	Solution heat-treatment	Artificial aging
Time in hour	0:10, 0:20, 0:30, 1:00, 2:00	1:00, 2:00, 4:00, 8:00, 12:00, 24:00, 48:00
Temperature in °C	300, 400, 500	140, 160, 180

2.4. Characterization and testing

Optical Microscope (OM, Zeiss Axio Imager 2) and Scanning Electron Microscope (SEM, Zeiss Auriga) were employed to examine the microstructure of non-heat-treated (NHT) and heat-treated (HT) specimens as well as the fracture surfaces. Electron Backscatter Diffraction (EBSD, HKL Nordlys II Detector) and Energy-Dispersive X-ray (EDX) spectroscopy were used for the detailed analytical work; EBSD and EDX analyses provided information about the crystallographic orientation and chemical composition, respectively. Before characterizations, samples were polished down to 0.02µm (Buhler's MasterMet™ 2 suspension). No etching was necessary, as a scratch-free surface with sufficient image contrast could be achieved right after polishing.

3. Results and Discussion

3.1. Heat-treatment

It is well known that an increase in the ultimate tensile strength and the yield strength would enhance the fatigue life [17]. On the other hand, an increase in hardness indicates an increase in both ultimate and yield strength [18]. Therefore, to minimize the experimental effort and calibrate the heat-treatment process parameters to be applied to the specimens for mechanical tests, heat-treatment conditions associated with maximum hardness were selected. This ensures high strength and fatigue life after heat-treatments. The evolution of hardness during heat-treatment is shown in Figure 4.

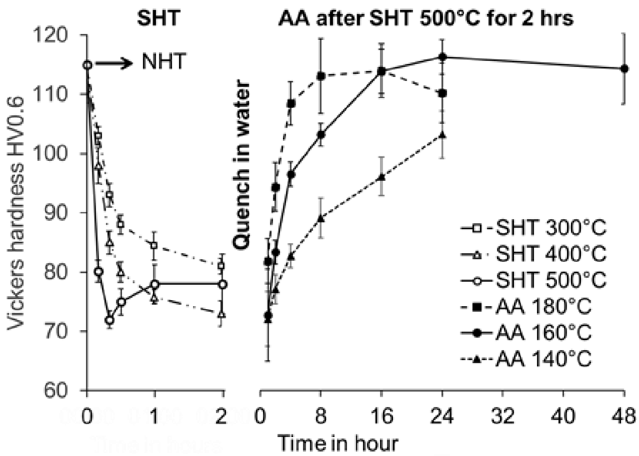

Figure 4. Micro-hardness evolution of the alloy during SHT at 300, 400, and 500°C followed by AA at 140, 160, and 180°C.

A relatively high hardness, i.e., 115HV, of AlSi10Mg alloy measured in NHT condition already shows an enhancement compared to its conventionally manufactured counterparts, 63HV [19], which agrees with the already published data [20]. This observation can be justified by the size of columnar and equiaxed grains, in the range of 10 to 70µm, compared to grain sizes of the order of a few hundred microns in conventionally cast AlSi10Mg [4]. Figure 5 shows the inverse pole figure (IPF) map of the α-Al matrix with a face-centered cubic crystal structure, which is the result of an EBSD analysis of the microstructure in the NHT condition. Despite the presence of equiaxed grains, much of the microstructure is composed of columnar grains with average length and thickness of 70±5µm and 10±2µm, respectively. Most columnar grains are oriented with their <001>

crystal direction parallel to the build direction. Such a texture has been widely reported in PBF-LB/M-manufactured AlSi10Mg alloy and many other metallic alloys processed by PBF-LB/M [21, 22]. This texture arises parallel to the heat extraction direction during columnar solidification of metallic alloys with cubic crystal structures [23]. Equiaxed grains with an average diameter of 8±2μm and a weaker texture than columnar grains can be observed near the borders of weld beads. The columnar zone is expected to have formed due to the rapid growth of grains with favorable <001> orientation parallel to the heat flow direction. In general, thermal gradient G and solidification rate R, at the solid-liquid interface determine the grain morphology during solidification and the morphology transition from equiaxed to columnar [24, 25]. In this study, the thermal gradient within the weld bead border is as high as 10^6K/m and the solidification rate behind the weld bead has the same speed as the scanning speed, 1.3 m/s, which can explain the rapid growth of grains parallel to the heat flow direction. Both the thermal gradient and solidification rate are calculated based on Rosenthal theoretical solution of moving heat source [26] at liquidus-solidus region.

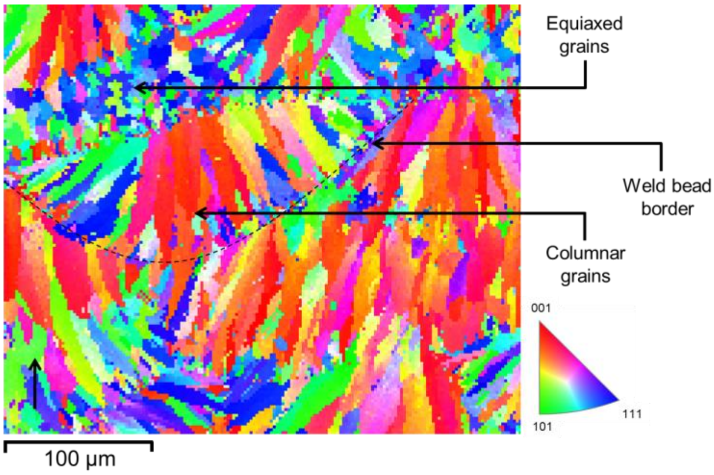

Figure 5. EBSD IPF map in the NHT condition. Colors indicate crystal directions parallel to the build direction. The black arrow indicates the build direction.

Furthermore, Si supersaturation of up to 2 to 7at. % has been reported during the PBF-LB/M of Al-Si alloys [27], while the equilibrium solubility of Si in Al is below 0.1at. % at room temperature. This high supersaturation contributes as well to hardness of the material in the NHT condition. Consequently, grain refinement (Hall-Petch strengthening) and solid solution strengthening resulting from the high solidification rate [1] are both considered as the primary factors for the relatively high hardness of the NHT PBF-LB/M material [28]. In addition, the Orowan strengthening due to the presence of a high density of dispersed Si particles at grain and sub-grain boundaries is also expected to have contributed to the high hardness [29].

After SHT at 500°C for only a few minutes, the material became considerably softer. The micro-hardness rapidly decreased to 72HV within 20 minutes before reversing to 78 HV after an hour of SHT at 500°C. An initially sharp drop of hardness followed by a steady hardness level at longer holding times has also been reported by Aboulkhair [30]. This sharp reduction in hardness is due to the microstructure coarsening. Moreover, it is also expected that the amount of supersaturated Si in α-Al after quenching from 500°C be lower than that in the NHT condition [31], thereby diminishing the solid solution strengthening. The small reversion of hardness after 20 minutes at 500°C could be attributed to the partial dissolution of coarse intermetallic components and therefore slight solid solution strengthening due to an increase in the solute amounts of elements such as Fe and Si. It is necessary to point out that the hardness decrease was more gradual for SHT at lower temperatures of 400 and 300°C.

The influence of AA at 140, 160, and 180°C after two hours of SHT followed by water quenching can also be seen in Figure 4. At 160°C, the hardness increases to 116HV after 24 hours. The slight hardness decrease after longer aging times indicates the onset of over-aging. When aged at 140°C, the material could not reach to its peak hardness condition yet in 24 hours. On the other hand, when the alloy was aged at 180°C, its hardness reached a maximum of 114HV only after 16 hours, followed by a relatively sharp drop in hardness due to over-aging. Consequently, for further investigation of the tensile and fatigue behavior of the alloy, an AA time of 24 hours and temperature of 160 °C was selected.

The microstructure in the NHT and HT conditions are shown in Figure 6 and Figure 7. As can be seen, weld bead borders and the three distinct areas, which were visible in NHT condition with "fish scale" morphology [32] [33] [34] can hardly be identified in HT condition. The three distinct areas are fine sub-grains of pro-eutectic (primary) α-Al in center of weld bead, larger sub-grains on the border of weld bead and heat-affected zone with broken intercellular network. Similar results have been reported in several publications [35, 36, 31]. These weld bead borders disappear through compositional and microstructural homogenization during SHT. The coalescence and coarsening of Si particles during the SHT, as implied from the microstructure in the HT condition, leads to the dissolution of Si-rich eutectic regions. Irregular-shaped Si particles with sizes in the range of 0.2 and 4μm can clearly be observed in HT condition (Figure 7). All these would imply the weakening of anisotropic microstructure and mechanical properties of the NHT PBF-LB/M material fabricated either parallel or perpendicular to the build platform. Moreover, several plate-like precipitates with a length of 4±1μm are distributed in the microstructure. SEM-EDX analyses indicated high concentrations of Fe in the precipitates. These precipitates are expected to be β-Al_5SiFe [29].

The increase in hardness from 72 to 116HV after 24 hours of artificial aging at 160°C, can be explained by precipitation hardening. Aging is initiated by the formation of Guinier–Preston zones (GP zones) rich in Mg and Si, followed by the formation of metastable phases, e.g., β'' and β', which eventually evolve to nanoscale β-Mg_2Si precipitates [5]. It is also interesting to note that the weight fraction of pro-eutectic α-Al in NHT condition is much higher than what is predicted from the phase diagram under equilibrium, namely 65wt.% compared to the equilibrium fraction of only 24wt.%. This observation can be attributed to the non-equilibrium nature of the PBF-LB/M processes.

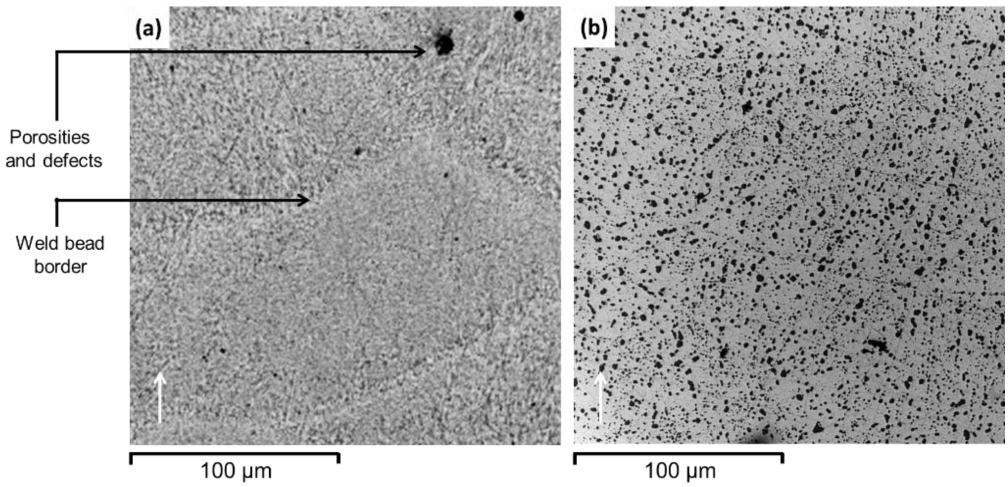

Figure 6. Cross-sectional optical micrograph of (a) NHT and (b) HT specimens. The white arrow indicates the build direction.

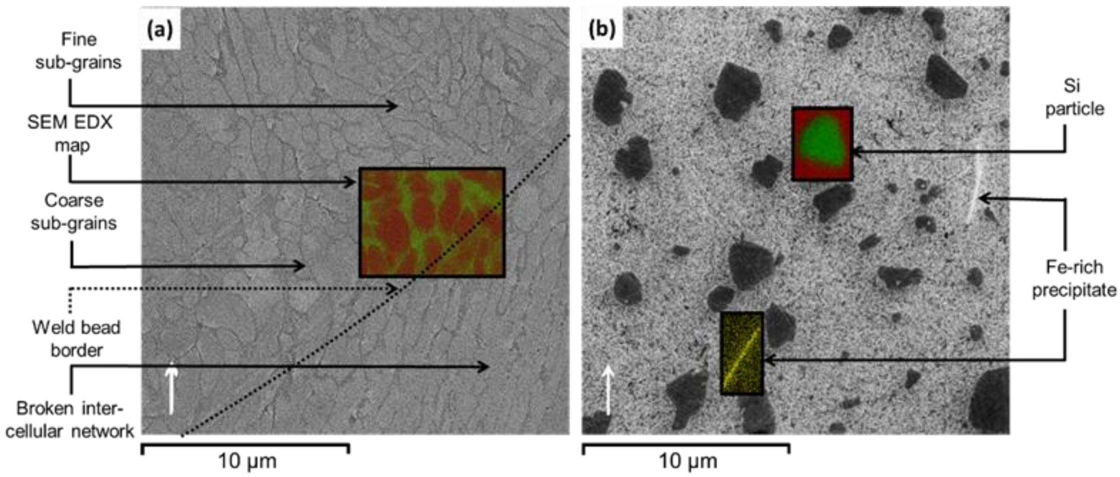

Figure 7. SEM results showing a cross-section of the NHT specimen. The white arrow represents the building direction. EDX map of Al (red) and Si (green) distribution in the area marked by a rectangle is superimposed.

3.2. *Tensile*

Figure 8 represents engineering tensile stress-strain curves for NHT and HT specimens. For each condition, the average tensile properties are summarized in Table 4. The results indicate an improvement in both yield strength and ductility in the HT condition. The high work hardening rate of NHT material is due to the presence of dislocations inherent to PBF-LB/M (see texture gradients in NHT, Figure 5). These preexisting dislocations facilitate yielding but they tangle quickly leading to a high work hardening rate. Another contribution might have arisen from the partitioning of strain between α-Al and eutectic regions of the material in NHT condition. It could be expected that the strain is rather localized in the softer α-Al and the strain localization is then manifested as rapid work hardening. A similar observation has also been reported in [37].

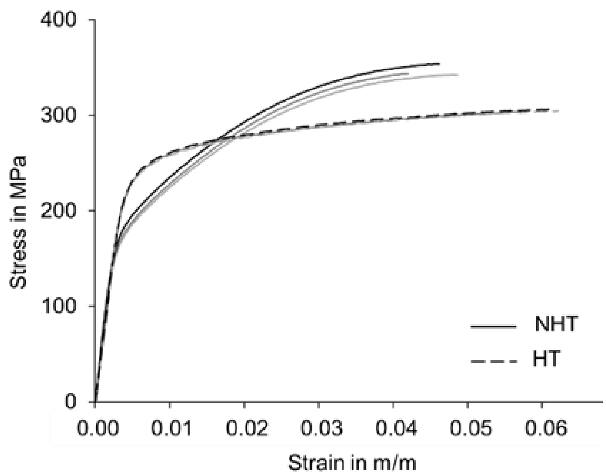

Figure 8. Engineering tensile stress-strain curves for the NHT and HT conditions.

Table 4. Tensile properties in NHT and HT conditions.

	$R_{p0.2}$ in MPa	σ_{UTS} in MPa	$\varepsilon_{fracture}$ in %
NHT	187±3	347±5	4.5±0.3
HT	240±3	305±3	6.0±0.3

Typically, in structural metals such as Al-Si alloys, an increase in the strength compromises the ductility, also known as the strength-ductility trade-off [38]. In the present case however, like the work of Hitzler et al. [39], both yield strength and ductility improved. Three arguments can explain the simultaneous improvement in both strength and ductility after the heat-treatment. Firstly, the recovery occurring during heat-treatment reduces the residual stresses accumulated in the alloy during PBF-LB/M processing. This lowers the fracture probability because of locally excessive stresses and increases the ductility after heat-treatment. Secondly, the fine-grains of the NHT material remain intact after SHT, thus preserving the impact of the Hall-Petch strengthening factor. Finally, Mg_2Si precipitation further contributes to strengthening. Different results have been observed in other publications as well. For instance, in [40] the T6 heat-treatment decreased the yield strength but improved the ductility. On the other hand, in [29], the treatment increased yield strength compared to the alloy in NHT condition. These differences may be due to the different fabrication process parameters, heat-treatment as well as other post-processing parameters, e.g., pre-heating temperature, stress relief process after printing, machining, and SHT and AA temperature and duration.

3.3. Fatigue

The S-N curves for the NHT and HT conditions during fully reversed loading (R = −1) are shown in Figure 9. The Wöhler curve was fitted according to the Basquin fatigue model, $S_a = a\,(N_f)^b$, where S_a is the stress amplitude, N_f is the number of cycles to failure, a and b are the fitting parameters. The survival probability P_s at 90% is depicted as envelope around the fitted curves as well. The resulted curves show that the heat-treatment significantly improved the fatigue life of the alloy in both low and high cyclic loads. The calculated fatigue strength at 10^7 cycles (S_N) for the specimens in HT conditions is approximately 80MPa, which shows an increase of 60% from NHT fatigue strength of 50MPa. An increase in S_N in the HT condition has also been observed in [41], where 50MPa and 75MPa fatigue strength is reported in NHT and HT condition. However, slightly dissimilar results have also been reported [42]. Differences are likely related to the employment of various fabrication process parameters as well as T6 heat-treatment parameters in individual studies. In contrast to conventionally cast products, fabrication parameters and heat-treatment conditions are currently not well established. It is also important to note the increase in the value Basquin slope (b) in post heat-treatment from -0.16 to -0.19. It illustrates that while there is an overall improvement of fatigue behavior in all stress amplitudes, a greater improvement occurs in the low cyclic fatigue behavior.

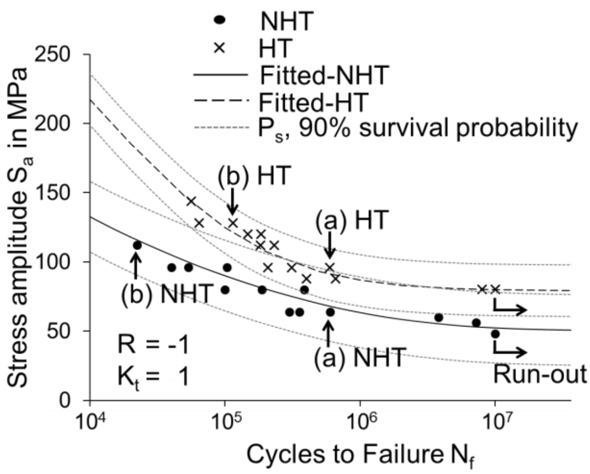

Figure 9. S-N curves for the NHT and HT conditions. All tests were performed at stress ratio R = -1 and stress concentration factor K_t = 1. P_s denotes the 90% survival probability. The four specimens selected for fractography are marked with letters a and b (see Figure 11 and Figure 12).

To obtain a complete picture of the influence of the increased yield stress after heat-treatment on fatigue life, the modified Goodman method [43] is employed and the fatigue endurance diagram is plotted (see Figure 10). The method reduces the experimental effort by providing an estimate of the fatigue life at different R-values based on one set of measurements at R=-1. This form of representation enables to compare the results of this work with already published data based on measurements performed at different R-values. In this figure, the knowledge of mechanical properties under tensile loading conditions and S_N under fully reversed cyclic loading in the axial direction is used to predict the fatigue performance of materials in NHT and HT conditions under cyclic loading conditions with non-zero mean stress (S_m). It is evident that despite a slight decrease in the ultimate tensile strength, the fatigue life region is expanded by 90% in the HT condition, which is due to the increase in the yield strength after heat-treatment. Moreover, the influence of heat-treatment is more pronounced in the negative S_m range.

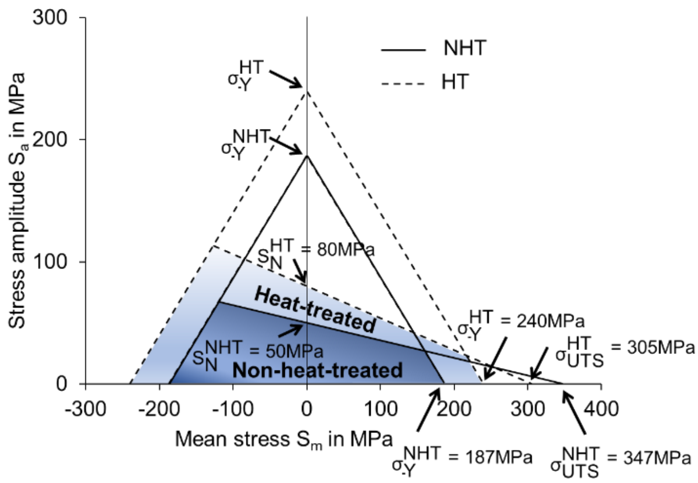

Figure 10. Modified Goodman diagram for both NHT and HT materials. Yield, ultimate tensile and fatigue strengths are marked by σ_Y, σ_{UTS}, and S_N, respectively.

3.4. Fractography

In order to describe better the connection between fatigue properties and features of the fracture surface, e.g., the size, type, and location of defects as well as crack initiation and propagation regions, detailed fractography analyses were conducted. Fracture surfaces for two specimens in the NHT condition under Sa = 64 and 112MPa (Figure 11) and two HT specimens under Sa = 96 and 128MPa (Figure 12) were examined. The main zones of crack initiation (i), crack propagation (ii), transition area (iii) as well as the final overload fracture (iv) can be observed clearly for all specimens. These zones have been observed by other studies as well [44, 45]. The influence of applied S_a on all stages of fracture evolution can be seen, where at lower stresses the fatigue crack propagation and transition region are larger compared to the specimens tested under higher stresses.

In most cases, the crack initiates from one defect with size of around 100 to 150µm on the surface of the specimens. However, as shown in Figure 11(b), only at extremely high applied S_a, e.g., 112MPa, multiple crack initiation sites, i.e., cleavage fans, were observed, rather like the ones reported in [44]. The initiating defects are irregular in shape while other non-critical smaller defects, i.e., gas pores, remain spherical (Figure 11(a)). Looking closer, one can detect un-melted aluminum powders within the initiating defects, which indicates lack of fusion (Figure 11(b)).

Preprints (www.preprints.org) | NOT PEER-REVIEWED | Posted: 2 April 2021 doi:10.20944/preprints202104.0075.v1

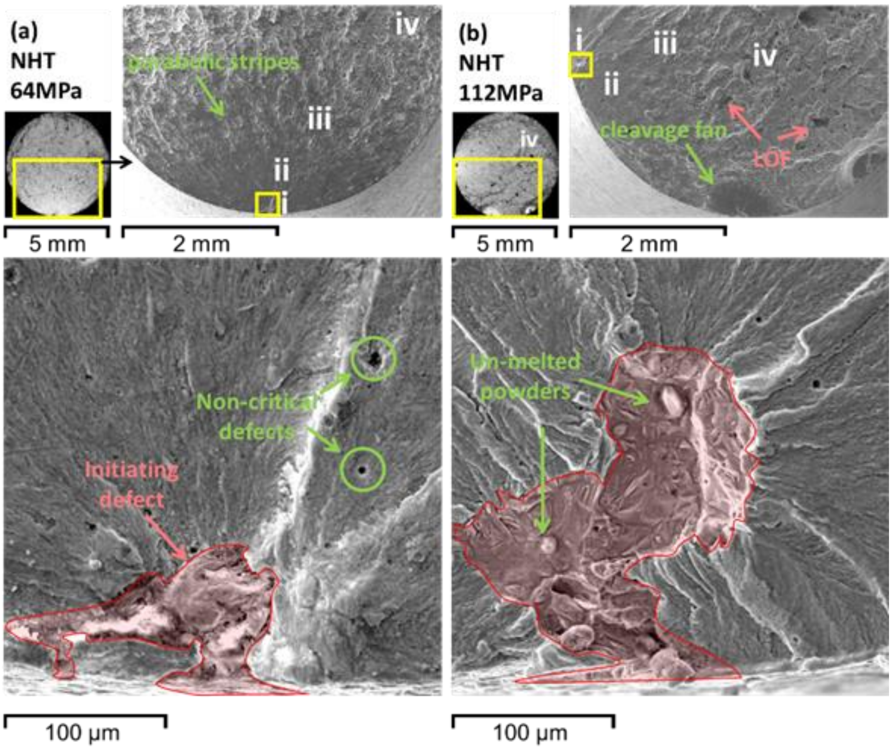

Figure 11. Fracture surfaces of (a) and (b) two NHT specimens marked by letters a and b. Top-left: Light microscopy images of the whole fracture surface. Top-right: SEM micrograph of the crack initiation and propagation zones. Below: defects responsible for the fatigue fracture initiation.

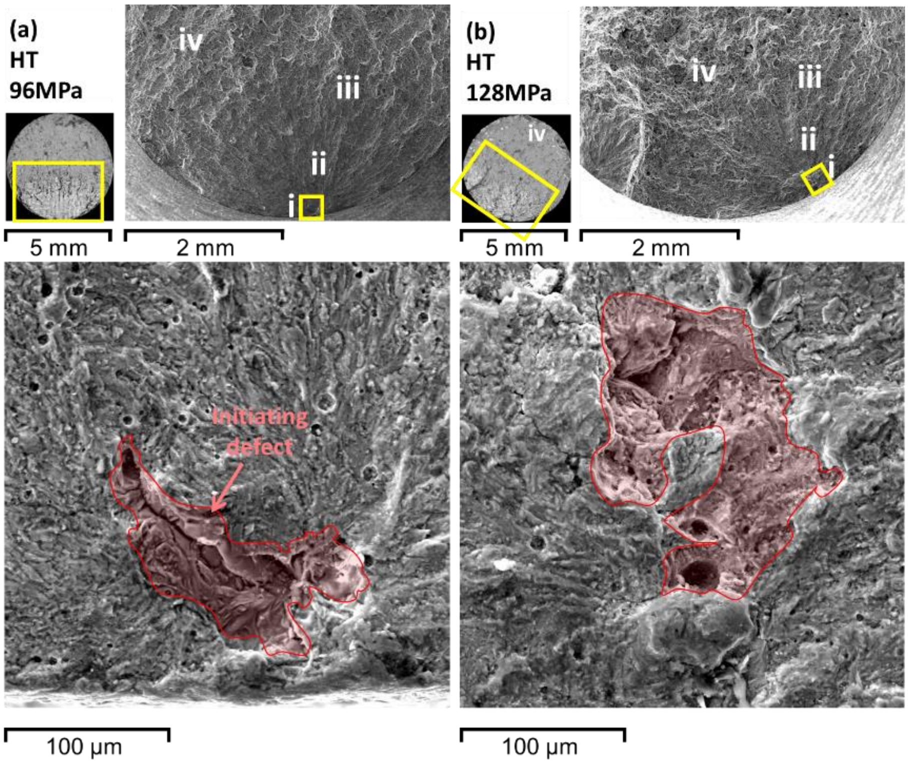

Figure 12. Fracture surfaces of (a) and (b) two HT specimens marked by letters a and b. Top-left: Light microscopy images of the whole fracture surface. Top-right: SEM micrograph of the crack initiation and propagation zones. Below: defects responsible for the fatigue fracture initiation.

Preprints (www.preprints.org) | NOT PEER-REVIEWED | Posted: 2 April 2021 doi:10.20944/preprints202104.0075.v1

In fatigue propagation region, a relatively smooth surface, due to repeated compression of the crack, can be observed. In the transition area between crack propagation and final overload fracture, parabolic stripes can be identified signifying the propagation direction (see Figure 13). At the center of each stripe, a defect could consistently be found. These defects, which are away from the main initiating defect on the surface of the specimens, induce a minor crack initiation and propagation. These cracks can then merge to the main crack propagating on a different plane and form these small parabolic stripes [46].

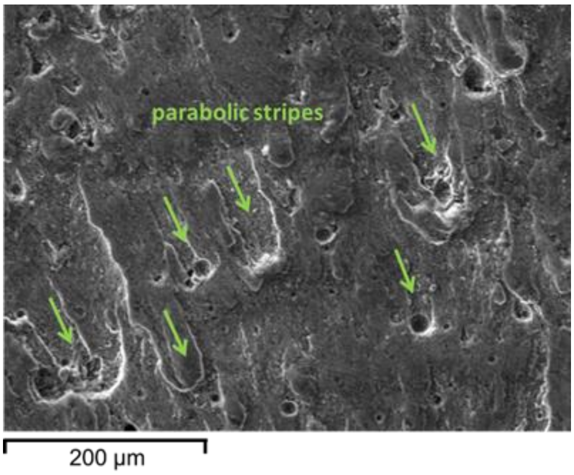

Figure 13. Fractography at the transition zone between crack initiation and propagation zone of NHT specimens.

In the overload region, large irregular defects due to lack of fusion (LOF) can be observed. At higher magnifications, a quasi-cleavage pattern, i.e., small cleavage facets and dense shear ridges mixed with dimple regions are visible in the crack propagation zone of the fracture surface, indicating quasi-brittle fracture of NHT specimens (see Figure 14(a)). After heat-treatment, as discussed in section 3.1., the columnar dendritic α-Al sub-grains are fully eliminated, and the eutectic Si network evolves into larger Si particles. Larger dimples are more pronounced on the fracture surface of the HT specimens, indicating an increase in ductility, and hence an improvement in low cycle S_N of the HT alloys (see Figure 14(b)).

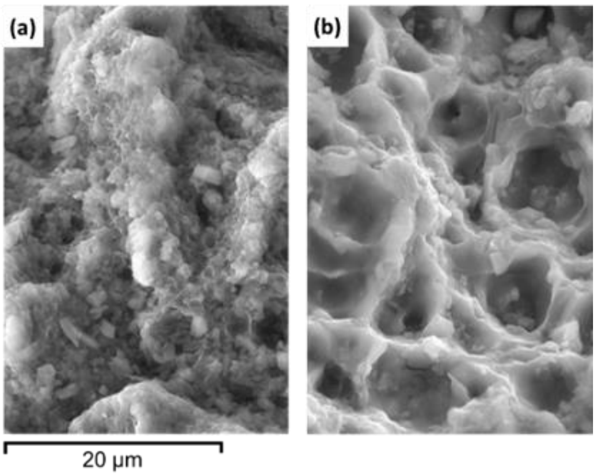

Figure 14. Fractography at the final overload zone of (a) NHT and (b) HT specimens.

 doi:10.20944/preprints202104.0075.v1

5. Conclusions

Based on the results obtained in this study for the AlSi10Mg alloy, the following conclusions can be drawn:

1- The microstructure of the NHT material is mainly composed of columnar grains oriented with their <001> crystal direction parallel to the build direction, which is due to the existence of a high thermal gradient within the border of the weld bead.

2- SEM results for the NHT condition indicated a weight fraction of primary α-Al higher than the equilibrium content. This is caused by the rapid solidification conditions. Additionally, the non-equilibrium nature of the process suppresses the growth of secondary dendritic arms in α-Al.

3- A relatively high hardness of 115HV was measured for the NHT condition. It is due to the presence of exceptionally fine grains and a high concentration of supersaturated alloying elements within the aluminum matrix. Another contributing factor to the high hardness is the presence of fine Si particles at the grain and sub-grain boundaries. It is also worth mentioning that since hardness associated with plastic deformation, good work hardening characteristic of the NHT material, as shown in the tensile test results, must have contributed to its high hardness.

4- Solution heat-treatment at 500°C for two hours followed by quenching and then artificial aging at 160°C for 24 hours was selected after performing a series of parametric studies to bring the alloy to its peak-hardened condition. After the heat-treatment, columnar dendritic sub-grains, as well as weld bead border, disappear through compositional homogenization, which implies the elimination of the anisotropic microstructural and mechanical properties of the NHT material. At peak-hardened condition, the hardness of 116HV was measured which is primarily caused by precipitation hardening of the alloy with nanoscale β-Mg_2Si precipitates.

5- The flow curves indicate a simultaneous improvement of both yield strength and tensile elongation in HT condition. This can be explained very well by the following effects; firstly, the residual stress accumulated in the specimen during PBF-LB/M process is recovered after the heat-treatment, thus reducing the probability of fracture in regions of the NHT specimen under high local stresses. Secondly, the impact of the Hall-Petch strengthening factor is preserved after heat-treatment, as the grain size after SHT remains like that of in NHT condition. Lastly, Mg_2Si precipitation further contributes to strengthening.

6- Although there is a slight decrease in the ultimate tensile strength, fatigue life after heat-treatment is improved because of an increase in the yield strength. Moreover, in both NHT and HT specimens, fatigue failure is initiated from large defects located just below or on the specimen surface for all stress levels. The heat-treatment did not have much influence on the size of initiating defects, which were typically of the order of 100 to 150μm.

7- The fracture mechanism after heat-treatment changes from quasi-brittle to a more ductile type. Fracture surface examinations indicated that the quasi-cleavage pattern of the alloy in the NHT condition converts into relatively larger dimples in the crack propagation zone in the HT condition.

Author Contributions: Mr. Sajadi carried out the main characterization and analyses of the data and wrote original draft of the paper. Mr. Tiemann and Mr. Darabi partly performed the tensile and fatigue tests. Ms. Bandari conducted the SEM and EBSD imagining. Dr. Mola supported with the conceptualization as well as refining the project idea and methodology, and edited the manuscript. Prof. Schmauder supervised the project, reviewed the manuscript and made the final editing.

Funding: This research received no external funding.

Acknowledgments: The authors gratefully acknowledge the support of their colleagues at the Institute of Laser Technologies (IFSW), University of Stuttgart, and the infrastructure made available by TRUMPF GmbH + Co. KG in the ARENA2036 e.V. research building for the fabrication of the samples.

Conflicts of Interest: The authors declare no conflict of interest. The funders had no role in the design of the study; in the collection, analyses, or interpretation of data; in the writing of the manuscript, or in the decision to publish the results.

References

1. C. Yan, L. Hao, A. Hussein, P. Young, J. Huang, W. Zhu, „Microstructure and mechanical properties of aluminium alloy cellular lattice structures manufactured by direct metal laser sintering," *MaterialsScience&Engineering A,* Bd. 628, pp. 238-246, 2015.
2. D. Dai, D. Gu, R. Poprawe, M. Xia, „Influence of additive multilayer feature on thermodynamics, stress and microstructure development during laser 3D printing of aluminum-based material," *Science Bulletin,* Bd. 62, pp. 779-787, 2017.
3. J. Kadkhodapour, H. Montazerian, A.Ch. Darabi, A.P. Anaraki, S.M. Ahmadi, A.A. Zadpoor, S. Schmauder, „Failure mechanismsofadditivelymanufactured porous biomaterials:Effectsofporosity and typeofunitcell," *Journal of the Mechanical Behavior of Biomedical Materials,* Bd. 50, pp. 180-191, 2015.
4. L. Girelli, M. Tocci, M. Gelfi, A. Pola, „Study of heat treatment parameters for additively manufactured AlSi10Mg in comparison with corresponding cast alloy," *Materials Science and Engineering A,* Bd. 739, pp. 317-328, 2019.
5. X. Larrávoz Izcara, A. Guirao Blank, F. Pyczak, P. Staron, S. Schumann, N. Huber, „Characterization and modeling of the influence of artificial aging on the microstructural evolution of age-hardenable AlSi10Mg(Cu) aluminum alloys," *Materials Science and Engineering A,* Bd. 610, pp. 46-53, 2014.
6. S. Romano, A. Brückner-Foit, A. Brandão, J. Gumpinger, T. Ghidini, S. Beretta, „Fatigue properties of AlSi10Mg obtained by additive manufacturing: Defect-based modelling and prediction of fatigue strength," *Engineering Fracture Mechanics,* Bd. 187, pp. 165-189, 2018.
7. F. Trevisan, F. Calignano, M. Lorusso, J. Pakkanen, A. Aversa, E.P. Ambrosio,M. Lombardi, P. Fino, D. Manfredi, „On the Selective Laser Melting (SLM) of the AlSi10Mg Alloy: Process, Microstructure, and Mechanical Properties," *Materials,* Bd. 10, p. 76, 2017.
8. N. Aboulkhair, I. Maskery, C. Tuck, I. Ashcroft, N.M. Everitt, „Improving the fatigue behaviour of a selectively laser melted aluminium alloy: Influence of heat treatment and surface quality," *Materials & Design,* Bd. 104, pp. 174-182, 2016.
9. B. Mfusi, N. Mathe, L. Tshabalala and P. Popoola, „The Effect of Stress Relief on the Mechanical and Fatigue Properties of Additively Manufactured AlSi10Mg Parts," *Metals,* Bd. 9, p. 1216, 2019.
10. S. Beretta, M. Gargourimotlagh, S. Foletti, A. du Plessis and M. Riccio, „Fatigue strength assessment of "as built" AlSi10Mg manufactured by SLM with different build orientations," *International Journal of Fatigue,* Bd. 139, p. 105737, 2020.
11. M. Tang and P. Pistorius, „Fatigue life prediction for AlSi10Mg components produced by selective laser melting," *International Journal of Fatigue,* Bd. 125, pp. 479-490, 2019.
12. L. Zhuo, Z. Wang, H. Zhang, E. Yin, Y. Wang, T. Xu and C. Li, „Effect of post-process heat treatment on microstructure and properties of selective laser melted AlSi10Mg alloy," *Materials Letters,* Bd. 234, pp. 196-200, 2019.
13. H. Wadell, „Volume, shape, and roundness of rock particles," *The Journal of Geology,* Bd. 40, Nr. 5, pp. 443-451, 1932.
14. S.E. Brika, M. Letenneur, C.A. Dion, V. Brailovski, „Influence of particle morphology and size distribution on the powder flowability and laser powder bed fusion manufacturability of Ti-6Al-4V alloy," *Additive Manufacturing,* Bd. 31, p. 100929, 2020.
15. Laura Cordova, Mónica Campos and Tiedo Tinga , „Revealing the Effects of Powder Reuse for Selective Laser Melting by Powder Characterization," *JOM,* Bd. 71, pp. 1062-1072, 2019.
16. W. E. Frazier, „Metal Additive Manufacturing: A Review," *Journal of Materials Engineering and Performance,* Bd. 23, pp. 1917-1928, 2014.
17. George Ellwood Dieter, David Bacon, Mechanical Metallurgy, McGraw-Hill, 1988.
18. E.J. Pavlina, C. Vantyne, „Correlation of Yield Strength and Tensile Strength with Hardness for Steels," *Journal of Materials Engineering and Performance,* Bd. 17, pp. 888-893, 2008.
19. L. Girelli, M. Tocci, M. Gelfi, A. Pola, „Study of heat treatment parameters for additively manufactured AlSi10Mg in comparison with corresponding cast alloy," *Materials Science and Engineering: A,* Bd. 739, pp. 317-328, 2019.
20. A.H. Maamoun, Y.F. Xue , M.A. Elbestawi, S.C. Veldhuis, „The Effect of Selective Laser Melting Process Parameters on

the Microstructure and Mechanical Properties of Al6061 and AlSi10Mg Alloys," *Materials*, Bd. 12, p. 12010012, 2018.

21. A. Hadadzadeh, B.S. Amirkhiz, A. Odeshi, M. Mohammadi, „Dynamic loading of direct metal laser sintered AlSi10Mg alloy: Strengthening behavior in different building directions," *Materials & Design*, Bd. 159, pp. 201-211, 2018.
22. M.L. Montero-Sistiaga, R. Mertens, B. Vrancken, X. Wang, B. V. Hooreweder, J. Kruth, J. Van Humbeeck, „Changing the alloy composition of Al7075 for better processability by selective laser melting," *Journal of Materials Processing Technology*, Bd. 238, pp. 437-445, 2016.
23. M. Flemings, Solidification processing, material science and thechnology, Wiley Verlag, 2006.
24. A. Hadadzadeh, B.S. Amirkhiz, J. Li, M. Mohammadi, „Columnar to equiaxed transition during direct metal laser sintering of AlSi10Mg alloy: effect of building direction," *Additive Manufacturing*, Bd. 23, pp. 121-131, 2018.
25. J. Hunt, „Steady state columnar and equiaxed growth of dendrites and eutectic," *Materials Science and Engineering*, Bd. 65, pp. 75-83, 1984.
26. D. Rosenthal, „Mathematical Theory of Heat Distribution during Welding and Cutting," *Welding Journal*, Bd. 20, pp. 220-234, 1941.
27. J. Wu, X. Wang, W. Wang, M. Attallah, M. Loretto, „Microstructure and strength of selectively laser melted AlSi10Mg," *Acta Materialia*, Bd. 117, pp. 311-320, 2016.
28. T. Maeshima, K. Oh-ishi, „Solute clustering and supersaturated solid solution of AlSi10Mg alloy fabricated by selective laser melting," *Heliyon*, Bd. 5, Nr. 2, p. e01186, 2019.
29. L. Zhou, A. Mehta, E. Schulz, B. McWilliams, K. Cho, Y. Sohn, „Microstructure, precipitates and hardness of selectively laser melted AlSi10Mg alloy before and after heat treatment," *Materials Characterization*, Bd. 143, pp. 5-17, 2018.
30. N. Aboulkhair, C. Tuck, I. Ashcroft, I. Maskery, N. Everitt, „On the Precipitation Hardening of Selective Laser Melted AlSi10Mg," *Metallurgical and Materials Transactions A*, Bd. 46, pp. 3337-3341, 2015.
31. A. Iturrioz, E. Gil, M. M. Petite, F. Garciandia, A. M. Mancisidor, M. San Sebastian, „Selective laser melting of AlSi10Mg alloy: influence of heat treatment condition on mechanical properties and microstructure," *Welding in the World*, Bd. 62, p. 885–892, 2018.
32. I. Rosenthal, A. Stern, N. Frage, „Microstructure and Mechanical Properties of AlSi10Mg Parts Produced by the Laser Beam Additive Manufacturing (AM) Technology," *Metallography, Microstructure, and Analysis*, Bd. 3, pp. 448-453, 2014.
33. M. Nahmanya, I. Rosenthalb, I. Benishtia, N. Frageb, A. Stern, „Electron beam welding of AlSi10Mg workpieces produced by selected selectedlaser melting additive manufacturing technology," *Additive Manufacturing*, Bd. 8, pp. 63-70, 2015.
34. H. Asgaria, C. Baxtera, K. Hosseinkhanib, M. Mohammadi, „On microstructure and mechanical properties of additively manufactured AlSi10Mg_200C using recycled powder," *Materials Science & Engineering A*, Bd. 707, pp. 148-158, 2017.
35. X. Liu, C. Zhao, X. Zhou, Z. Shena,W. Liu, „Microstructure of selective laser melted AlSi10Mg alloy," *Materials and Design*, Bd. 168, p. 107677, 2019.
36. C. Silbernagel, I. Ashcroft, P. Dickens, M. Galea, „Electrical resistivity of additively manufactured AlSi10Mg for use in electric motors," *Additive Manufacturing*, Bd. 21, pp. 395-403, 2018.
37. L. Hitzler, C. Janousch, J. Schanz, M. Merkel, B. Heine, F. Mack, W. Hall, A. Öchsner, „Direction and location dependency of selective laser melted AlSi10Mg specimens," *Journal of Materials Processing Technology*, Bd. 243, pp. 48-61, 2017.
38. R. Ritchie, „The conflicts between strength and toughness," *Nature Materials*, Bd. 10, pp. 817-822, 2011.
39. L. Hitzler, A. Charles, A. Öchsner, „The Influence of Post-Heat-Treatments on the Tensile Strength and Surface Hardness of Selective Laser Melted AlSi10Mg," *Defect and Diffusion Forum*, Bd. 370, pp. 171-176, 2017.
40. M. Fousová, D. Dvorský, A. Michalcová, D. Vojtěch, „Changes in the microstructure and mechanical properties of additively manufactured AlSi10Mg alloy after exposure to elevated temperatures,," *Materials Characterization*, Bd. 137, pp. 119-126, 2018.
41. S. Bagherifard, N. Beretta, S. Monti, M. Riccio, M. Bandini, M. Guagliano, „On the fatigue strength enhancement of additive manufactured AlSi10Mg parts by mechanical and thermal post-processing," *Materials & Design*, Bd. 145, pp. 28-41, 2018.
42. C. Zhang, H. Zhu, H. Liao, Y. Cheng, Z. Hu, X. Zeng, „Effect of heat treatments on fatigue property of selective laser melting AlSi10Mg," *International Journal of Fatigue*, Bd. 116, pp. 513-522, 2018.
43. J. Goodman, Mechanics applied to engineering, Longmans, Green, 1919.
44. N. Uzan, R. Shneck, O. Yeheskel, N. Frage, „Fatigue of AlSi10Mg specimens fabricated by additive manufacturing

selective laser melting (AM-SLM)," *Materials Science and Engineering A,* Bd. 704, pp. 229-237, 2017.

45. E. Beevers, A.D. Brandão, J. Gumpinger, M. Gschweitl, C. Seyfert, P. Hofbauer, T. Rohr, T. Ghidini, „Fatigue properties and material characteristics of additively manufactured AlSi10Mg – Effect of the contour parameter on the microstructure, density, residual stress, roughness and mechanical properties," *International Journal of Fatigue,* Bd. 117, pp. 148-162, 2018.

46. Z.W. Xu, Q. Wang, X.S. Wang, C.H. Tan, M.H. Guo, P.B. Gao, „High cycle fatigue performance of AlSi10mg alloy produced by selective laser melting," *Mechanics of Materials,* Bd. 148, p. 103499, 2020.